J. Mech. Phys. Solids 167 (2022) 104993

Contents lists available at ScienceDirect

Journal of the Mechanics and Physics of Solids

journal homepage: www.elsevier.com/locate/jmps

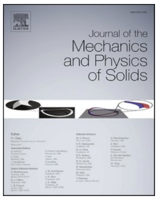

Linear stability analysis of the condition for vibration during frictional slip

Kyungjae Im [a,*], Jean-Philippe Avouac [a,b]

[a] *Division of Geological and Planetary Science, California Institute of Technology, Pasadena, CA 91125, United States*
[b] *Division of Engineering and Applied Science, California Institute of Technology, Pasadena, CA 91125, United States*

ABSTRACT

Slip along a frictional contact between elastic bodies can be stable or unstable, leading to stick-slip motion. Frictional slip can also be associated with vibrations. The condition for these vibrations and their characteristics remains poorly understood. To address this issue, which is relevant to engineering and earth science, we carry out a linear stability analysis of a spring-and-slider system obeying rate and state friction. We first identify the solution space for the linearized equation and define the conditions for different slip modes from the real and imaginary parts of the solution. We then derive asymptotic equations for all boundaries between overdamped stable sliding, inertial/non-inertial underdamped oscillation, stick-slip, and harmonic vibration. Finally, we verified the conditions with numerical simulations. Our work provides rigorous criteria regarding the conditions for the various frictional slip modes and the emergence of vibrations. It can help design appropriate approaches for suppressing undesired vibrations in mechanical systems and investigate the mechanisms generating vibrations (tremor) associated with fault slip in nature.

1. Introduction

Sliding along a solid contact is governed by friction and can be stable or unstable, leading to stick-slip (Rabinowicz, 1956), depending on the friction parameters, which govern the strength drop during slip, and elastic properties, which govern unloading during slip (Rice and Ruina, 1983). Stick-slip is commonly observed at a slow loading rate for various materials, including rocks (Brace and Byerlee, 1966), plastic (Ben-David et al., 2010), rosin (Smith and Woodhouse, 2000), paper (Heslot et al., 1994), and articular joints (Lee et al., 2013). It has also long been recognized that frictional slip can be associated with high-frequency harmonic vibration (Brockely and Ko, 1970). Vibrations are commonly observed in rapidly slipping systems (Brockley and Ko, 1970; Ibrahim, 1994), for example, vehicle brake systems (brake squeal) (e.g., Kinkaid et al., 2003) or musical instruments (Smith and Woodhouse, 2000).

Until recently, the stick-slip and inertial vibration have been mostly independently investigated or often not distinguished due to the distinct circumstances for their emergence. For instance, geoscientists have been exclusively interested in the stick-slip phenomenon due to the extremely low tectonic loading rate (order of $\sim 10^{-9}$ m/s), which favors stick-slips (i.e., earthquakes (Brace and Byerlee, 1966)) rather than vibration. Conversely, inertial vibrations are of interest for rapidly slipping mechanical systems since it causes damage to the sliding material (Ibrahim, 1994). However, tremor signals observed in natural volcanic (Chouet, 1996; Dmitrieva et al., 2013) and non-volcanic systems (Obara 2002; Shelly et al., 2007) can be explained by friction-induced vibrations (Im et al., 2019; Im and Avouac, 2021). Similarly, friction-induced vibrations in mechanical systems can be explained with the frictional framework commonly used to explain earthquakes (Cabboi et al., 2016). In both cases, the emergence of vibrations is explained by rate and state friction (RSF).

Rate and state friction (RSF) is a phenomenological law established based on laboratory observations, which includes velocity-

---

[*] Corresponding author.
E-mail address: kjim@caltech.edu (K. Im).

https://doi.org/10.1016/j.jmps.2022.104993
Received 29 March 2022; Received in revised form 8 June 2022; Accepted 17 June 2022

dependent effects ("rate" effect) and history of sliding surface effect ("state" effect) (e.g., Marone, 1998). It was initially developed to explain rock friction (Dieterich, 1979) and recognized later on to apply to various solid contact such as glass, metal, wood, plastic, and paper (Dieterich and Kilgore, 1994; Heslot et al., 1994), as well as nanoscale contacts (Tian et al., 2018). RSF must result from the mechanisms governing deformation at the scale of the asperities where the two bodies are in contact (e.g., Molinari and Perfettini, 2019). The RSF formalism seems to apply widely, although these mechanisms probably vary depending on the material and condition (pressure, temperature, fluid content). RSF has been widely used in geoscience to explain fault slip and earthquakes (e.g., Tse and Rice, 1986; Scholz, 1998; Lapusta et al., 2000). The RSF was also recognized as a relevant formalism in the tribology community (Vakis et al., 2018). Initially, the RSF explains stick-slip phenomena (Rice and Tse 1986; Baumberger and Caroli, 2006). Recently, the RSF formalism has been adopted to study mechanical vibrations as well (Cabboi et al., 2016; Im et al., 2019). Viesca (2016) noted the existence of non-inertial vibrations in a one-dimensional interface with RSF.

Slip motion with RSF is governed by non-linear differential equations. Linearization of the equations provides a first-order estimation of the slip behavior, although we acknowledge a higher-order stability analysis would be possible (e.g., Nosyreva and Molinari, 1998) and could provide further insight since linear instability does not always imply non-linear instability. The transition from stable to unstable sliding within RSF is well explained by the linearization of the spring slider system (Rice and Ruina, 1983) and one-dimensional interface (Rice et al., 2001; Viesca, 2016). Vibrations can actually emerge in both slip modes (Im and Avouac, 2021). The emergence of vibration apparently depends on inertia and the system stiffness (Im et al., 2019; Im and Avouac, 2021), but the dependence on both of these factors was not explicated in these previous studies.

Here, we carry out a linear stability analysis to characterize how vibrations emerge during slip governed by rate and state friction. We first describe the linearization of the equations describing the force balance and rate and state friction. Then we derive the criteria for transition between stick-slip to inertial vibration and critical damping point, where inertial vibration starts to appear in a stable sliding regime. Finally, the analytic expressions for stability transition and vibration emergence are verified via numerical solutions.

2. Stability and vibration emergence

We consider a simple spring-slider system. The stability of the spring-slider system with rate and state friction has been analyzed in previous studies (Rice and Ruina, 1983; Baumberger and Caroli, 2006). This section reviews the rate and state friction law and presents a linear stability analysis expanded to account for vibrations.

2.1. Rate and state friction law and stability transition

In the rate and state frictional framework, friction is dependent on sliding velocity and frictional state (Dieterich, 1979; Marone, 1998). The most common form of RSF writes

$$\mu = \mu_0 + a\ln\left(\frac{V}{V_0}\right) + b\ln\left(\frac{V_0\theta}{D_c}\right) \tag{1}$$

where V is velocity, θ is state variable, μ_0 is a reference friction coefficient at reference velocity V_0, D_c is a critical slip distance, and a and b are empirical constants, generally positive, describing the magnitude of the direct and evolution effects, respectively. Adopting a regularized form of RSF (Rice and Ben-Zion, 1996; Lapusta et al., 2000) to avoid the singularity at $V = 0$ would make no difference to the study presented here.

The evolution of the state variable (θ) is commonly described by either the 'aging law' (Dieterich, 1979),

$$\frac{d\theta}{dt} = 1 - \frac{V\theta}{D_c} \tag{2}$$

or the 'slip law' (Ruina, 1983).

$$\frac{d\theta}{dt} = -\frac{V\theta}{D_c}\ln\left(\frac{V\theta}{D_c}\right) \tag{3}$$

For both evolution laws, $\theta_{ss}=D_c/V$ yields steady-state friction with $\mu_{ss}=\mu_0+(a-b)\ln(V/V_0)$. Given that the first-order expansion of $-x\ln(x) \approx 1-x$ near $x = 1$, the two evolution laws behave similarly for a small velocity perturbation near steady-state ($V\theta/D_c \sim 1$), indicating that the linearized equation near the steady-state for both evolution laws are also identical. The two equations diverge when the system is far from steady-state. The state variable evolves at a non-zero velocity in the slip law, while the aging law implies maximum healing in a static system ($V = 0$; $b > 0$ implies a logarithmic increase of friction with time).

The equation of motion of the spring-slider system at constant loading velocity V_0 is,

$$\frac{M\ddot{\delta}}{\sigma} = \frac{K(V_0t-\delta)}{\sigma} - \mu \tag{4}$$

where M is mass per unit area (kg/m^2), K is a stiffness expressed in units of shear stress (Pa/m), σ is normal stress, and δ is slider displacement. The system of equations Eqs. (1)–((4) can be linearized around the steady-state velocity V_0 with linearized variables $\delta(t) = \delta_0+V_0t + \Delta\delta(t)$ and $\theta(t) = \theta_{ss}+ \Delta\theta(t)$, where δ_0 is initial slider position at steady state (Baumberger and Caroli, 2006). The

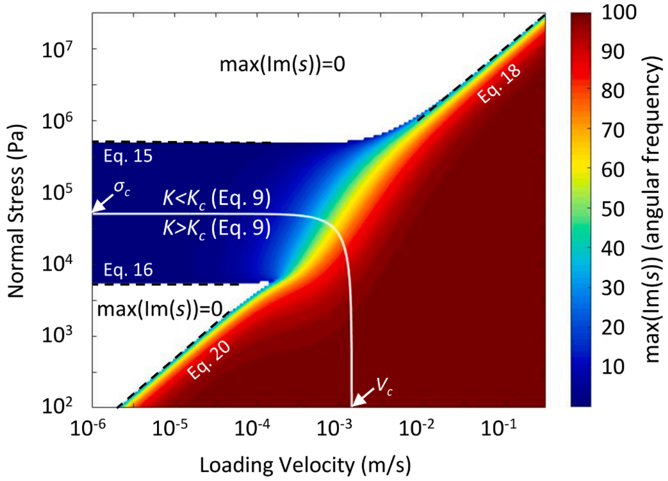

Fig. 1. Maximum value of imaginary solutions of Eq. (8) (with parameter $a = 0.004$, $b = 0.006$, $D_c = 10$ μm, $K = 10$ MPa/m, and $M = 1000$ kg/m^2). The uncolored area (max(Im(s))=0) represents where the imaginary part of all solutions is zero. The white line represents K=K_c, where stability transition occurs. The equations of four asymptote lines (black dashed lines) of max(Im(s))=0 are defined in the main text. The frequency contour is identical for the case of a-b>0 (i.e., intrinsically stable case) but without stability transition (white line).

linearized variables yield a system of linear equations

$$\frac{M\Delta\ddot{\delta}}{\sigma}+\frac{K\Delta\delta}{\sigma}+a\frac{\Delta\dot{\delta}}{V_0}+b\frac{V_0\Delta\theta}{D_c}=0 \tag{5}$$

$$\Delta\dot{\theta}=-\frac{V_0}{D_c}\Delta\theta-\frac{1}{V_0}\Delta\dot{\delta} \tag{6}$$

Eqs. (5) and (6) can be combined into

$$\frac{M}{\sigma}\Delta\dddot{\theta}+\left(\frac{a}{V_0}+\frac{MV_0}{\sigma D_c}\right)\Delta\ddot{\theta}+\left(\frac{K}{\sigma}+\frac{a-b}{D_c}\right)\Delta\dot{\theta}+\frac{KV_0}{\sigma D_c}\Delta\theta=0 \tag{7}$$

Solutions $\Delta\theta$ (also $\Delta\delta$) take form e^{st}. We get the following characteristic equation (also similarly presented by Baumberger and Caroli 2006),

$$\frac{M}{\sigma}s^3+\left(\frac{a}{V_0}+\frac{MV_0}{\sigma D_c}\right)s^2+\left(\frac{K}{\sigma}+\frac{a-b}{D_c}\right)s+\frac{KV_0}{\sigma D_c}=0 \tag{8}$$

The solutions of s are complex numbers. The real part of the solution, $Re(s)$, represents the excitation/attenuation of the motion, and the imaginary part of the solution, Im(s), defines the angular frequency ω, which is related to the ordinary frequency by $f= \omega/2\pi$, When $Re(s) < 0$, the amplitude of the motion attenuates (i.e., stabilizes), and when $Re(s) > 0$, it becomes linearly unstable.

The stability transition occurs when at least one of the solutions is pure imaginary (i.e., $Re(s) = 0$ with non-zero Im(s)). This occurs when (Rice and Ruina, 1983),

$$K=K_c=\frac{(b-a)\sigma}{D_c}\left[1+\frac{MV_0{}^2}{\sigma a D_c}\right] \tag{9}$$

Eq. (9) shows that the spring-slider system becomes unstable as velocity increases. The equation defines a critical stiffness, K_c, which can be written at the sum of a quasi-static critical stiffness

$$K_{c,qs}=\frac{(b-a)\sigma}{D_c} \tag{10}$$

and dynamic critical stiffness

$$K_{c,dyn}=\frac{(b-a)}{a}\frac{MV_0{}^2}{D_c{}^2} \tag{11}$$

For the given values of the rate and state friction parameters (a, b, & D_c), $K_{c,qs}$ is only dependent on normal stress (σ), and $K_{c,dyn}$ is only dependent on the kinetic energy ($\sim MV^2$).

The stability criterion, K=K_c, is presented as a curved line in the space of velocity - normal stress (white curve in Fig. 1) Im and

Avouac, 2021). Eqs. (10) and ((11) show that there exists a critical normal stress

$$\sigma_c = \frac{KD_c}{(b-a)} \tag{12}$$

and a critical velocity

$$V_c = D_c\sqrt{\frac{a}{b-a}}\sqrt{\frac{K}{M}} \tag{13}$$

The system becomes linearly unstable if either $V > V_c$ or $\sigma > \sigma_c$. Accordingly, the stability transition line (Fig. 1 white curve) has two asymptotes parallel to the y and x axis at $V = V_c$ and $\sigma = \sigma_c$, respectively (Fig. 1).

2.2. *Emergence of vibration – critical damping*

The imaginary part of the solution s represents angular frequency. Vibration may emerge if any of the solutions has a non-zero imaginary part. Since Eq. (8) is a simple cubic equation, Im(s) (or angular frequency) can be analytically calculated by the cubic formula at given normal stress and velocity. Fig. 1 shows the maximum value of the imaginary part of all solutions s of Eq. (8). Since imaginary solutions exist as a complex conjugate, $\max(\mathrm{Im}(s)) = 0$ indicates that all solutions have no imaginary part. There are two separate areas where imaginary parts of all three solutions are zero (Fig. 1 white area). One of them is within the unstable zone (high normal stress), and the other is within the stable zone (low normal stress).

Accordingly, the V- σ space can be divided into four different areas based on the sign of real and imaginary parts of the solution. (i) All solutions are pure negative real (white area with $K > K_c$ in Fig. 1). (ii) All solutions are negative real with any non-zero imaginary part (colored area with $K > K_c$ in Fig. 1). (iii) Any of the solutions has positive real with all imaginary parts of the solution being zero (white area with $K < K_c$). And (iv) Any of the solutions is positive real with any non-zero imaginary part (colored area with $K < K_c$). This areal division determines different modes of slip, such as under-damping, over-damping, stick-slip, and vibration. Since the stability transition criterion ($K = K_c$) is already defined (Eq. (9)), we now focus on the boundary of $\max(\mathrm{Im(s)}) = 0$ (white areas in Fig. 1) to define the criteria for slip mode change.

Four different asymptotes can be identified at the boundary of $\max(\mathrm{Im(s)}) = 0$ (black dashed lines in Fig. 1). The asymptotes can be derived analytically with some endmember assumptions. First, assuming inertia is negligible, the two horizontal dashed lines parallel to the $\sigma = \sigma_c$ can be derived. Consider a quasi-static system where $M = 0$. Then Eq. (8) becomes

$$\frac{a}{V_0}s^2 + \left(\frac{K}{\sigma} + \frac{a-b}{D_c}\right)s + \frac{KV_0}{\sigma D_c} = 0 \tag{14}$$

It can be seen that the real part of the solutions of Eq. (14) vanishes when $K = (b\text{-}a)\sigma/D_c$ (i.e., $M = 0$ in Eq. (9)), which is equal to the quasi-static critical stiffness. It can also be seen that the imaginary part of this simple quadratic equation vanishes at

$$\sigma = \frac{KD_c}{\left(\sqrt{b} - \sqrt{a}\right)^2} \tag{15}$$

and

$$\sigma = \frac{KD_c}{\left(\sqrt{b} + \sqrt{a}\right)^2} \tag{16}$$

These two normal stresses define Im(s)=0 boundaries in the quasi-static limit (horizontal dashed lines in Fig. 1). Note that the critical normal stress Eq. (12)) is the geometric mean of Eqs. (15) and ((16), making the distance of normal stress between Eqs. (15) and (12) identical to the distance between Eqs. (16) and (12) on a logarithmic scale, as shown in Fig. 1.

The two diagonal boundaries of max(Im(s)=0) in Fig. 1 approach linear asymptotes as velocity and normal stress tend to either infinity or zero. We find that the diagonal asymptote of Im(s)=0 in the unstable zone ($K < K_c$) can be derived by assuming $V_0 \rightarrow \infty$ and $\sigma \rightarrow \infty$ while V_0/σ is constant. With the assumptions, Eq. (8) becomes

$$Ms^2 + \frac{(a-b)\sigma}{V_0}s + K = 0 \tag{17}$$

The imaginary part of the solution vanishes at

$$\frac{2V_0\sqrt{MK}}{|a-b|\sigma} = 1 \tag{18}$$

Likewise, assuming $V_0 \rightarrow 0$ and $\sigma \rightarrow 0$ while V_0/σ is constant yields the equation of diagonal asymptote in the stable zone in Fig. 1. In this case, Eq. (8) becomes

$$Ms^2 + \frac{a\sigma}{V_0}s + K = 0 \tag{19}$$

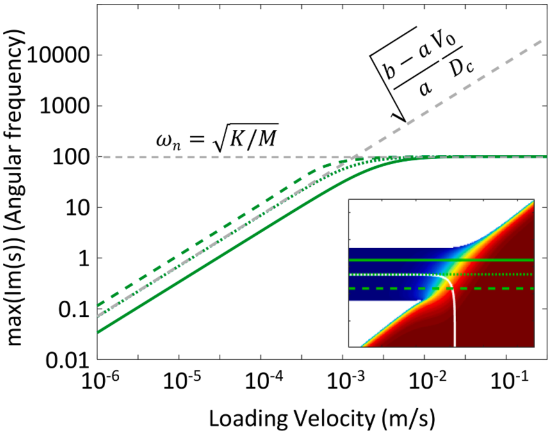

Fig. 2. The imaginary part of the solution max(Im(s)) at constant normal stresses. Three normal stresses are selected: σ_c (dotted line), $3\sigma_c$ (solid line), and $\sigma_c/3$ (dashed line) (see inset). Inset is an identical plot to Fig. 1 with indications of the location of the three normal stresses chosen for the plot.

Eq. (19) is identical to Eq. (17) except for '*a-b*' replacing '*a*' in the second term of the equation. The imaginary part of all solutions vanishes at

$$\frac{2V_0\sqrt{MK}}{a\sigma} = 1 \tag{20}$$

Eq. (20) is similar to Eq. 18 but is now independent of b. Eqs. (17) and (19) can also be obtained by assuming $D_c \to 0$ and $D_c \to \infty$ in Eq. (8), representing the unstable and stable endmembers respectively. The Eqs. (18) and (20) are the asymptotes of the two diagonal boundaries of max(Im(s)) $= 0$ (Fig. 1).

It is worth noting that the vibration emergence criteria are independent of a sign of *a-b* Eqs. (15), ((16), (18), and (20)). Accordingly, even if we change a and b value so that $a\text{-}b > 0$, we expect identical asymptotes for max(Im(s))=0 boundaries to the $a\text{-}b < 0$ case. However, the stability transition boundary (Eq. (9)) is dependent on the sign of *a-b*. Since K is always positive, there cannot be a stability transition when $a\text{-}b > 0$. Hence if $a\text{-}b>0$, the system is always linearly stable.

2.3. Frequency

The value of the imaginary part of the solution gives the angular frequency of the vibration motion. Fig. 1 shows that within a wide area, the angular frequency is close to but not higher than 100 /s (red area in Fig. 1) at high loading velocity or low normal stress. Given that our input parameter $K = 10$ MPa/m and $M = 1000$ kg/m^2, the 100 /s is identical to natural angular frequency $\omega_n = \sqrt{K/M}$. This is consistent with the numerical observation of Im et al. (2019) that, as loading velocity increases, the vibration frequency rapidly approaches the natural frequency but doesn't exceed it.

The emergence of the natural frequency at high loading velocity (V_0) and low normal stress (σ) may be understood by considering Eq. (8). If $V_0 \to \infty$ then the equation becomes equivalent to

$$Ms^2 + K = 0. \tag{21}$$

The solution of this equation is $s = \pm i\sqrt{K/M}$, which yields harmonic vibration at the natural frequency. Similarly, when the normal stress is very low, $\sigma \to 0$, Eq. (8) becomes equivalent to

$$Ms^3 + \frac{MV_0}{D_c}s^2 + Ks + \frac{KV_0}{D_c} = 0 \tag{22}$$

This equation also has two pure imaginary solutions $s = \pm i\sqrt{K/M}$. These results show that the motion approaches harmonic vibration at high velocity or low normal stress. Note that the frequency is dependent on the mass, and therefore the vibration is inertial.

The blue zone around the transition from stable sliding to stick-slip, which is bounded by the normal stresses given by Eqs. (15) and (16) (Fig. 1), shows that, in that domain, vibrations have a frequency much lower than the natural frequency. The frequency in this area can be estimated by calculating the frequency at stability transition. Substituting critical stiffness (Eq. (9)) into Eq. (8) yields two pure imaginary solutions (Baumberger and Caroli, 2006)

$$s = \pm i\sqrt{\frac{b-a}{a}\frac{V_0}{D_c}} \tag{23}$$

Eq. (23) is the frequency at the stability transition (i.e., along the white line in Fig. 1 or Fig. 2 inset). It shows that the frequency of the solution is linearly dependent on the velocity and can be very small at a small loading velocity. Fig. 2 compares the frequency on

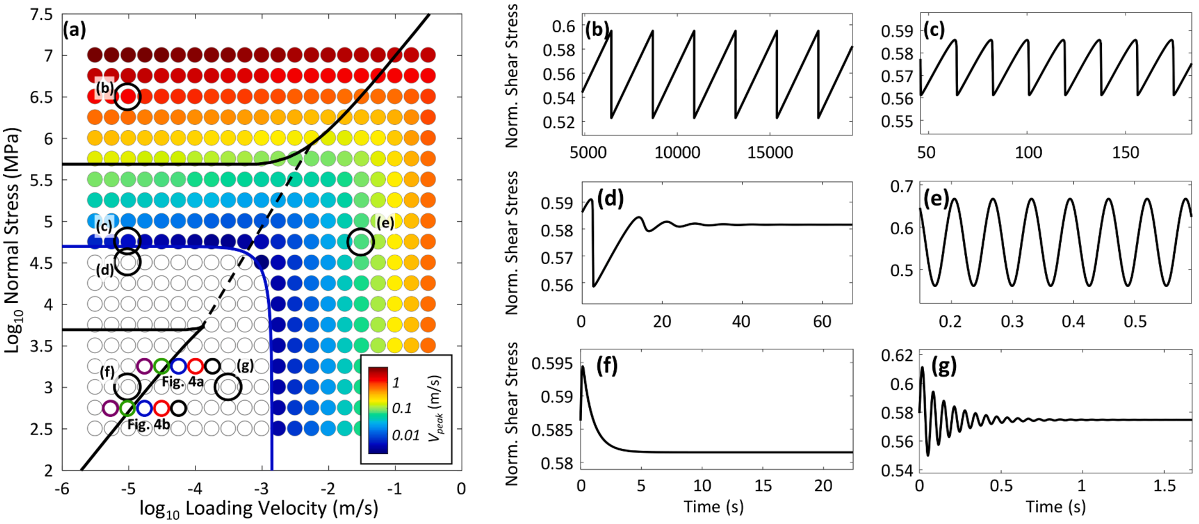

Fig. 3. Comparison of the results from the stability analysis (the boundaries of the different domains are reported in Fig. 1) with numerical simulations of the spring-slider system with the slip evolution law (circles) with varying loading velocity (x-axis) and normal stress (y-axis). Simulations are conducted with parameters identical to those used to generate Fig. 1 ($a = 0.004$, $b = 0.006$, $D_c = 10$ μm, $K = 10$ MPa/m, and $M = 1000$ kg/m^2). Initial velocity is set at 1/10 of each loading velocity. (a): Peak velocity (color of circles) of unstable slip at the periodic motion. The gray circles represent stable slip. The black circles correspond to the particular cases shown in (b–g). Colored empty circles in the stable zone denote the cases shown in Fig. 4. (b–g): Shear stress changes vs. time of the selected cases (loading rate and normal stress are represented in panel a).

three selected normal stress (green lines in Fig. 2 inset) and Eq. (23). Eq. (23) corresponds to the frequency at $\sigma=\sigma_c$ (green dotted line) at a low loading rate. In the low-frequency area (blue area in inset), max(Im(s)) increases with velocity until it reaches its natural frequency. Before it reaches the natural frequency, the frequency is independent of inertial parameters (*i.e.*, mass or stiffness), implying that the vibration in the transition between stick-slip to stable sliding (the low-frequency blue area in Fig. 1) is non-inertial.

3. Characteristics of slip mode – comparison to numerical solution

The mode of frictional sliding can be characterized based on the stability transition criterion ($K=K_c$), the condition for the emergence of a vibration (max(Im(s))>0), and its frequency (inertial or non-inertial). For example, if the system is stable ($K>K_c$) with a non-zero imaginary part of the solution (max(Im(s))>0), one expects stable sliding with attenuating oscillations. If the system is unstable ($K<K_c$) with all zero imaginary parts of the solution, one expects stick-slip rather than an inertial vibration.

Here we show that the slip mode observed in numerical simulations can indeed be explained with the criteria introduced in the previous sections. We used a numerical solver of a spring-slider with rate and state friction presented by Im et al. (2017). All simulations are conducted with friction parameter and stiffness identical to the values used in the previous section ($a = 0.004$, $b = 0.006$, $D_c = 10$ μm, $K = 10$ MPa/m, and $M = 1000$ kg/m^2). Initial velocity is set at 1/10 of loading velocity to generate velocity perturbations. We used the slip law (Eq. (3)) for state evolution, but as discussed earlier (and also discussed by Im et al. 2019), the slip mode transition criteria are identical for the aging law (Eq. (2)) since the linearized equations are identical for both evolution laws. The negative a-b value (a-b=−0.002) represents the potentially unstable system. We also investigated an intrinsically stable system, where a-b>0 (a-b = 0.002).

3.1. Potentially unstable system (a-b < 0)

In the potentially unstable system (a-b<0), the steady-state friction (or resistance) decreases as velocity increases, enabling unstable sliding. The previous section shows that frictional sliding becomes unstable at high normal stress or high velocity (Eq. (9)). We showed that the solution of the linearized equation of the potentially unstable system could be divided into four different areas with the combinations of the real and imaginary parts of the solutions (Fig. 1). On top of this, we can add an approximate boundary line (Fig. 3a dashed line), which separates the high-frequency zone (red area in Fig. 1) and the low-frequency zone (blue area in Fig. 1). Then the V-σ space is divided into 6 different zones corresponding to different regimes (Fig. 3a). We carried out systematic simulations to check the consistency with the analytical boundaries derived from our stability analysis and chose some case examples to illustrate the behavior observed in each domain (Fig. 3b–g). Fig. 3a shows the peak velocity of spring-slider simulations in the potentially unstable system ($a = 0.004$, $b = 0.006$, $D_c = 10$ μm) over a 5-order of magnitude range of normal stress and loading velocity. The results are consistent with the stability criteria (Eq. (9); blue line in Fig. 3a). All simulations with $K<K_c$ show unstable sliding (colored circles), and all simulation results with $K>K_c$ show stable sliding (empty circles). The peak velocity is low near the stability criteria (blue line) and increases as the normal stress and loading velocity increase.

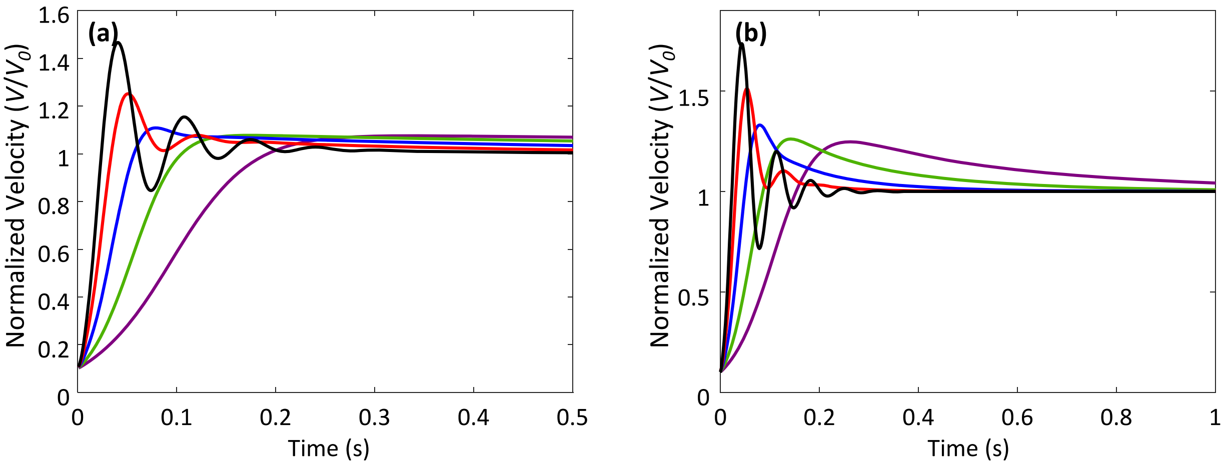

Fig. 4. Slip velocity of selected numerical simulations at normal stress $10^{3.25}$MPa (panel a) and $10^{2.75}$MPa (panel b). The normal stress and loading rate of each case are shown as colored circles in Fig. 3a with the same color as in the figure. The velocity is normalized by the loading rate.

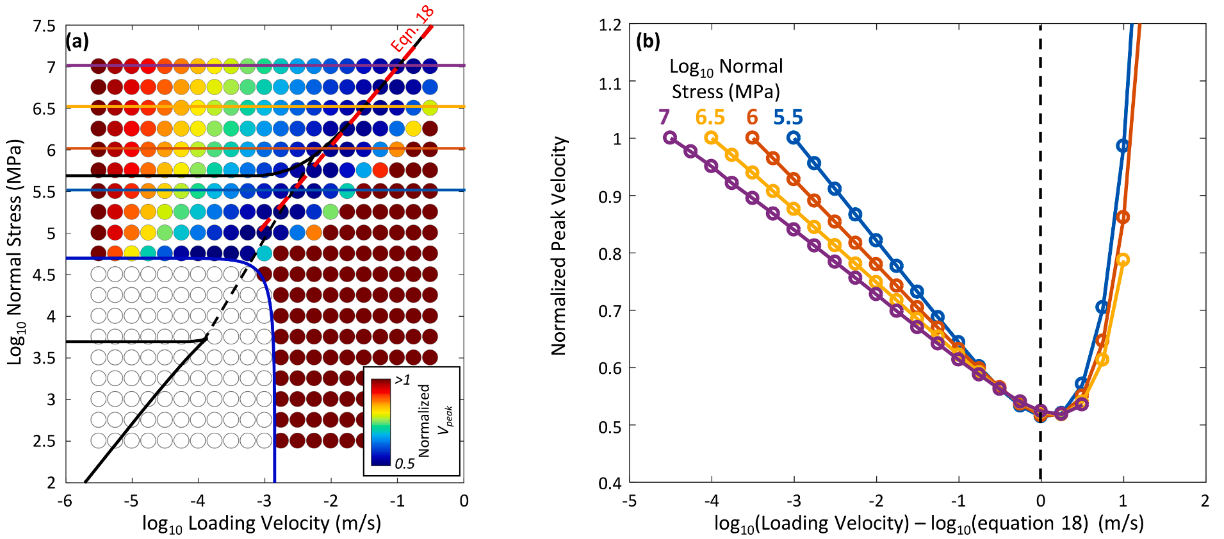

Fig. 5. Peak velocity normalized by the peak velocity at $V_l = 10^{-5\cdot}5$ m/s. (a): All normalized peak velocity. Colored horizontal lines represent the case shown in panel b. The red dashed line denotes Eq. (18). (b). Normalized peak velocity vs. loading velocity adjusted by Eq. (18). Zero at the x-axis represents the loading velocity at Eq. (18). Colors denote different normal stress cases shown as a horizontal line in panel a.

Individual cases (Fig. 3b–g) show distinct characteristics of sliding motions at each regime depending on the stability transition ($K<K_c$ or $K>K_c$) and the frequency (max(Im(s))=0, $<<\omega_n$, or $\approx\omega_n$, where ω_n is natural angular frequency).

1 Unstable ($K<K_c$) and max(Im(s))=0. Fig. 3b is in this category and shows unstable sliding. (slip mode: stick-slip)
2 Unstable ($K<K_c$) and 0<max(Im(s))$<<\omega_n$. Fig. 3c is in this category and also shows stick-slip instability. (slip mode: stick-slip)
3 Stable ($K>K_c$) and 0<max(Im(s))$<<\omega_n$. Fig. 3d is in this category and show low-frequency (non-inertial) attenuating vibration. (slip mode: non-inertial underdamped oscillation)
4 Unstable ($K<K_c$) and max(Im(s))$\approx\omega_n$. Fig. 3e is in this category and shows harmonic vibration at the natural frequency. (slip mode: harmonic vibration)
5 Stable ($K>K_c$) and max(Im(s))=0. Fig. 3f is in this category and shows stable sliding without oscillation (slip mode: overdamped stable slip)
6 Stable ($K>K_c$) and max(Im(s)) $\approx\omega_n$. Fig. 3g is in this category and shows natural frequency (inertial) attenuating vibration (slip mode: inertial underdamped oscillation)

The frequency of inertial harmonic vibrations (case 4&6 or Fig. 3e and g) corresponds to the natural frequency of the system (ω_n=100 /s, period 0.0625 s). The vibration frequency is limited to the natural frequency, as shown in Fig. 1. The two stick-slip cases

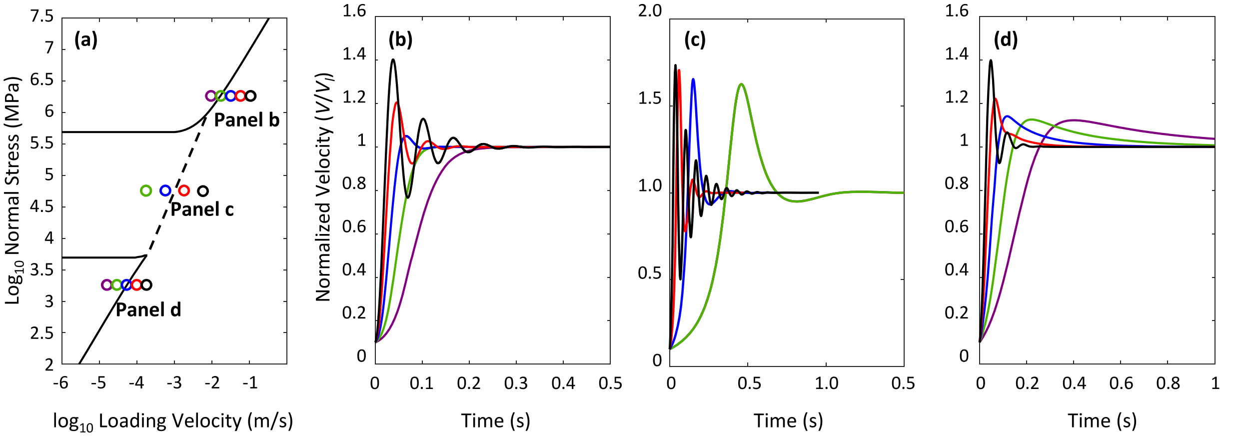

Fig. 6. (a): Map of slip characteristics in the intrinsically stable system (a-b)>0. We used parameters identical to those used in the simulations of the potentially unstable system (Figs. 1–5) but with $a = 0.006$ and $b = 0.004$. In this case, the stability transition does not exist. In the intrinsically stable system, all simulations show stabilized sliding. The colored circles represent the cases shown in panels (b–d). (b–d): Normalized velocity curves for the case denoted in panel a.

(cases 1&2 or Fig. 3b and c) are similar, although the slip events are smaller and more frequent in the case with the lower normal stress, as expected from the lower stress drop.

Defining the critical damping criterion, where the transition between overdamped and underdamped slip occurs, is important. It would define the optimal conditions to suppress undesired vibrations in a mechanical system. Fig. 3a shows that the critical damping points can be defined by Eqs. (16) and (20). Eq. (16) is a normal-stress-dependent critical damping point and is the boundary between overdamped stable slip and non-inertial underdamped oscillation. Conversely, Eq. (20) defines the velocity-dependent critical damping point and the boundary between overdamped stable slip and high-frequency inertial vibration. The high-frequency vibration might merit specific attention since, in mechanical systems, it can cause damage on the sliding surface (Ibrahim, 1994) and because the underdamped inertial vibration has been recently suggested as a potential mechanism for the generation of geologic tremor (Im and Avouac, 2021).

Fig. 4 shows selected simulation results across the velocity-dependent critical damping point. Both plots demonstrate that the high-frequency inertial vibration emerges when loading velocity is larger than the value defined by Eq. (20). In Fig. 4a and b, purple and green cases are in the overdamping area (Fig. 3a) and show no vibration motion. The blue cases, where the velocity is right above a critical damping point (Fig. 3a), present a subtle short-duration peak before stabilization. When the loading velocities are sufficiently larger than the critical damping point (e.g., red and black cases in Fig. 4), the simulations show attenuating harmonic vibrations. These observations confirm that Eq. (20) defines the critical damping point that determines the emergence of inertial vibration.

Im et al. (2019) identified the transition between stick-slip and harmonic vibration, but the analysis presented in that study was incomplete and not backed by the stability analysis presented in this study. Figs. 1 and 3 imply that the transition may occur at the condition expressed by Eq. (18). To test this, we normalized all peak velocities in Fig. 3a by the peak velocities at $10^{-5.5}$ m/s of each normal stress case (Fig. 5a). This normalization reveals that the minimum peak velocity at a given normal stress indeed occurs where Eq. (18) is satisfied (red dashed line Fig. 5a). This behavior is clearer if the x-axis is zeroed at the loading velocity given by Eq. (18) (Fig. 5b). In the RSF governed motion, as the loading rate increases, peak velocity decreases in the stick-slip domain (e.g., Vidale et al., 1994) but increases in the vibration domain (Im et al., 2019). Hence, the transition between stick-slip and inertial vibration occurs at the minimum peak velocity, which corresponds to the condition expressed by Eq. (18) (Fig. 5).

3.2. *Intrinsically stable system (a-b>0)*

An intrinsically stable system is defined by *a*-*b*>0. In this case, $K_c<0$ Eq. (9)), and accordingly, unstable sliding (i.e., $K<K_c$) is not allowed since spring coefficient K is always positive. So, all simulations yield stable slip regardless of normal stress and velocity. Hence, the stability transition ($K=K_c$ line) does not appear in the velocity-normal stress space (Fig. 6a). However, the boundaries for max(Im (s))=0 (or the vibration emergence) are still defined since their defining equations (Eqs. (15), ((16), (18), and (20)) are independent of the sign of *a*-*b*. Hence, the boundary asymptotes of max(Im(s))=0 in Fig. 6a are identical to that of Fig. 3a but without a stability transition line (Fig. 6a).

In this case, we only selected several cases over the max(Im(s))=0 boundaries to define the slip characteristics. The map has two max(Im(s))=0 zones at high and low normal stress, as in the case of a potentially unstable system. Since any combination of normal stress and loading velocity should produce stable sliding, it is expected that both boundaries for zero imaginary solution (solid black curves in Fig. 6a) would be critical damping points. This expectation is confirmed by velocity curves (Fig. 6b and d). If the loading velocities are sufficiently larger than the boundaries, simulations result in an attenuating vibration (black and red curves in Fig. 6b and d). Otherwise, the simulation results show overdamped stable sliding (purple curves in Fig. 6b and d). In the intrinsically stable system,

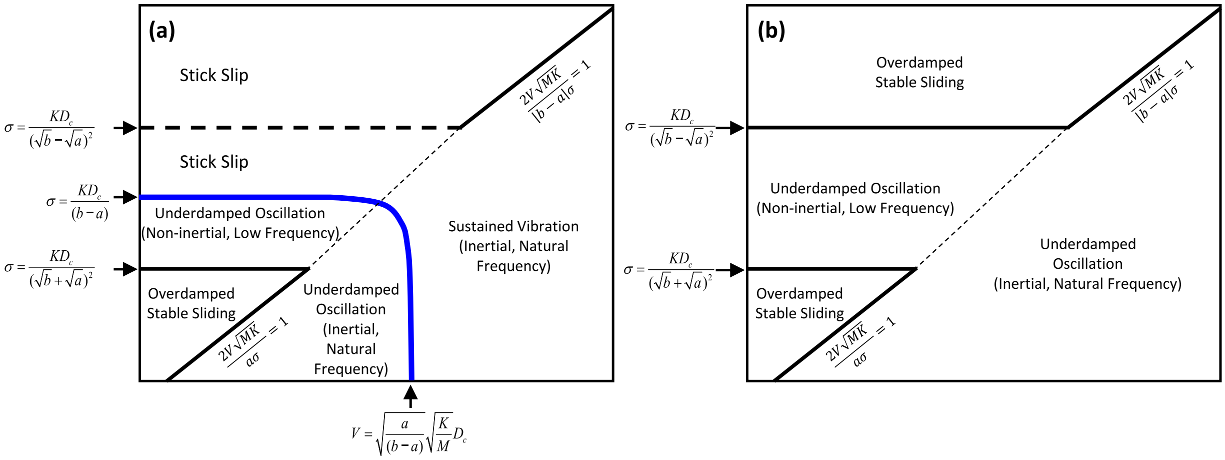

Fig. 7. Simplified map of sliding characteristics for (a) potentially unstable system and (b) intrinsically stable system.

all the Im(s)>0 boundaries correspond to critical damping.

Fig. 6c shows the transition from non-inertial underdamped oscillation to inertial underdamped oscillation. The non-inertial underdamped motions (green and blue in Fig. 6c) show only a mild pick and trough. However, as loading velocity increases, this motion changes into underdamped inertial oscillations (red and black curves in Fig. 6c).

4. Summary and conclusion

Our study shows that RSF frictional sliding, whether in the stick-slip or stable sliding regime, can be associated with vibrations of inertial or non-inertial origin. The different modes of frictional sliding identified in the study and their conditions are summarized with their asymptotic approximations shown in Fig. 7. In the potentially unstable system (Fig. 7a), the V-σ space can be divided into five zones: (i) overdamped stable sliding, (ii) non-inertial underdamped oscillation, (iii) inertial underdamped oscillation, (iv) stick-slip, and (v) harmonic vibration. In the intrinsically stable system (Fig. 7b), the V-σ space can be divided into four zones: (i) overdamped stable sliding at low normal stress, (ii) non-inertial underdamped oscillation, (iii) overdamped stable sliding at high normal stress, (iv) inertial underdamped oscillation.

Our linear stability analysis has limitations. A detailed description of the characteristics of stick-slip motion (Fig. 3b and c) cannot be derived from the linearized equations. Similarly, determining the precise frequency and amplitude of the low-frequency underdamped oscillations (Fig. 3d) would require a higher-order analysis. Non-linear stability analysis (e.g., Nosyreva and Molinari, 1998) would thus certainly provide further insight. However, the linear analysis provides a robust understanding of the conditions needed for vibrations associated with frictional slip, as shown by the comparison with the behavior observed in the numerical simulations.

This study confirms that the inertial parameter introduced by Im et al. (2019) $\eta = \frac{MV_0^2}{\sigma a D_c}$ yields an insufficient criterion ($\eta > 1$) for underdamped oscillation, as already mentioned in Im and Avouac (2021). The linear stability analysis actually leads to a different criterion (Eq. (20)). Both criteria imply that the vibration emerges when kinetic energy (MV^2) is high and normal stress and friction parameter 'a' is low. However, unlike the criterion, the criterion derived from Eq. (20) is independent of D_c but dependent on K.

We show that stick-slip, low-frequency oscillation, and high-frequency vibrations can result from system elastic response and inertia. The emergence of harmonic vibration from steady sliding is governed by Eq. (20), and it controls the unexpected vibrations in various mechanical systems and can also potentially explain tremors in volcanic and non-volcanic systems, pending a very low effective normal stress.

Rate and state friction law has been widely adopted in earth science due to its strong experimental support and applicability to earthquake mechanics (e.g., Scholz, 1998; Rice, 1993; Lapusta et al., 2000). On the other hand, it has received less attention in mechanical engineering, presumably because it is counterintuitive that time-dependent healing – a key feature needed to explain stick-slip motion – would be involved in the generation of vibrations. However, recently, it has been shown that the rate and state friction law can explain the vibration phenomenon (Cabboi and Woodhouse; 2018; Im et al., 2019). Here we present rigorous criteria for vibration emergence and show that the emergence of vibration depends on all the rate and state parameters (a, b, D_c), including the parameter b, which quantifies healing. Our work shows that both stick-slip and vibration can be explained by rate and state friction law but are just different responses from system elasticity and inertia.

CRediT authorship contribution statement

Kyungjae Im: Conceptualization, Methodology, Software, Writing – original draft. **Jean-Philippe Avouac:** Conceptualization, Validation, Writing – review & editing.

Declaration of Competing Interest

The authors declare that they have no known competing financial interests or personal relationships that could have appeared to influence the work reported in this paper.

Data Availability

No data was used for the research described in the article.

Acknowledgment

We thank one anonymous reviewer for the insightful comments and suggestions. We also benefitted from discussions with Rob Viesca. This study was supported by the National Science Foundation via the IUCR center Geomechanics and Mitigation of Geohazards (award #1822214) and NSF/EAR award #1821853.

References

Baumberger, T., Caroli, C., 2006. Solid friction from stick–slip down to pinning and aging. Adv. Phys. 55 (3–4), 279–348. https://doi.org/10.1080/00018730600732186.

Ben-David, O., Rubinstein, S.M., Fineberg, J., 2010. Slip-stick and the evolution of frictional strength. Nature 463 (7277), 76–79. https://doi.org/10.1038/nature08676.

Brace, W.F., Byerlee, J.D., 1966. Stick-slip as a mechanism for earthquakes. Am. Assoc. Adv. Sci. 153 (3739), 990–992. https://doi.org/10.1126/science.153.3739.990.

Brockley, C.A., Ko, P.L., 1970. Quasi-harmonic friction-induced vibration. J. Lubr. Technol. 550–556.

Cabboi, A., Woodhouse, J., 2018. Validation of a constitutive law for friction-induced vibration under different wear conditions. Wear 396, 107–125.

Cabboi, A., Putelat, T., Woodhouse, J., 2016. The frequency response of dynamic friction: enhanced rate-and-state models. J. Mech. Phys. Solids 92, 210–236.

Chouet, B.A., 1996. Long-period volcano seismicity: its source and use in eruption forecasting. Nature. https://doi.org/10.1038/380309a0.

Dieterich, J.H., 1979. Modeling of rock friction: 1. Experimental results and constitutive equations. J. Geophys. Res. 84 (9), 2161–2168.

Dieterich, J.H., Kilgore, B.D., 1994. Direct observation of frictional contacts: new insights for state-dependent properties. Pagoeph 143 (1–3), 283–302. https://doi.org/10.1007/BF00874332.

Dmitrieva, K., Hotovec-Ellis, A.J., Prejean, S., Dunham, E.M., 2013. Frictional-faulting model for harmonic tremor before Redoubt Volcano eruptions. Nat. Geosci. 6 (8), 652–656. https://doi.org/10.1038/ngeo1879.

Heslot, F., Baumberger, T., Perrin, B., Caroli, B., Caroli, C., 1994. Creep, stick-slip and dry-friction dynamics: experiments and a heuristic model. Phys. Rev. E 49 (6).

Ibrahim, R.A., 1994. Friction-induced vibration, chatter, squeal, and chaos Part I : mechanics of contact and friction. Appl. Mech. Rev. 47, 209–226.

Im, K., Avouac, J.P., 2021. Tectonic tremor as friction-induced inertial vibration. Earth Planet. Sci. Lett. 576, 117238 https://doi.org/10.1016/j.epsl.2021.117238.

Im, K., Elsworth, D., Marone, C., Leeman, J., 2017. The impact of frictional healing on stick-slip recurrence interval and stress drop: implications for earthquake scaling. J. Geophys. Res. Solid Earth. https://doi.org/10.1002/2017JB014476.

Im, K., Marone, C., Elsworth, D., 2019. The transition from steady frictional sliding to inertia-dominated instability with rate and state friction. J. Mech. Phys. Solids. https://doi.org/10.1016/j.jmps.2018.08.026.

Kinkaid, N.M., O'Reilly, O.M., Papadopoulos, P, 2003. Automotive disc brake squeal. J. Sound Vib. 267 (1), 105–166. https://doi.org/10.1016/S0022-460X(02)01573-0.

Lee, D.W., Banquy, X., Israelachvili, J.N., Zheng, G., 2013. Stick-slip friction and wear of articular joints. Proceedings of the National Academy of Sciences 110 (7), E567–E574.

Lapusta, N., Rice, J.R., Ben-Zion, Y., Zheng, G., 2000. Elastodynamic analysis for slow tectonic loading with spontaneous rupture episodes on faults with rate- and state-dependent friction. J. Geophys. Res. 105, 23765. https://doi.org/10.1029/2000JB900250.

Marone, C., 1998. Laboratory-derived friction laws and their application to seismic faulting. Annu. Rev. Earth Planet. Sci. 26 (1), 643–696. https://doi.org/10.1146/annurev.earth.26.1.643.

Molinari, A., Perfettini, H., 2019. Fundamental aspects of a new micromechanical model of rate and state friction. J. Mech. Phys. Solids 124, 63–82. https://doi.org/10.1016/j.jmps.2018.10.002.

Nosyreva, E.P., Molinari, A., 1998. Analysis of non-linear vibrations in metal cutting. Int. J. Mech. Sci. 40 (8), 735–748.

Obara, K., 2002. Nonvolcanic deep tremor associated with subduction in southwest Japan. Science 296 (5573), 1679–1681. https://doi.org/10.1126/science.1070378.

Rabinowicz, E., 1956. Stick and slip. Sci. Am. 194 (5), 109–119. https://doi.org/10.1038/scientificamerican0556-109.

Rice, J.R., 1993. Spatio-temporal complexity of slip on a fault. J. Geophys. Res. 98 (B6), 9885. https://doi.org/10.1029/93JB00191.

Rice, J.R., Lapusta, N., Ranjith, K., 2001. Rate and state dependent friction and the stability of sliding between elastically deformable solids. J. Mech. Phys. Solids 49 (9), 1865–1898. https://doi.org/10.1016/S0022-5096(01)00042-4.

Rice, J.R., Ruina, A.L., 1983. Stability of steady frictional slipping. J. Appl. Mech. 50 (2), 343. https://doi.org/10.1115/1.3167042.

Rice, J.R., Tse, S.T., 1986. Dynamic motion of a single degree of freedom system following a rate and state dependent friction law. J. Geophys. Res. 91 (1), 521–530.

Ruina, A., 1983. Slip instability and state variable friction laws. J. Geophys. Res. 88, 10359–10370.

Scholz, C.H., 1998. Earthquakes and friction laws. Nature 391 (6662), 37–42. https://doi.org/10.1038/34097.

Shelly, D.R., Beroza, G.C., Ide, S., 2007. Non-volcanic tremor and low-frequency earthquake swarms. Nature 446 (7133), 305–307. https://doi.org/10.1038/nature05666.

Smith, J.H., Woodhouse, J., 2000. The tribology of rosin. J. Mech. Phys. Solids 48 (8), 1633–1681. https://doi.org/10.1016/S0022-5096(99)00067-8.

Tian, K., Goldsby, D.L., Carpick, R.W., 2018. Rate and state friction relation for nanoscale contacts: thermally activated Prandtl-Tomlinson model with chemical aging. Phys. Rev. Lett. 120 (18), 186101.

Tse, S.T., Rice, J.R., 1986. Crustal earthquake instability in relation to the depth variation of frictional slip properties. J. Geophys. Res. 91 (B9), 9452. https://doi.org/10.1029/JB091iB09p09452.

Vakis, A.I., Yastrebov, V.A., Scheibert, J., Nicola, L., Dini, D., Minfray, C., …, Limbert, G., 2018. Modeling and simulation in tribology across scales: an overview. Tribol. Int. 125, 169–199.

Vidale, J.E., Ellsworth, W.L., Cole, A., Marone, C.J., 1994. Variations in rupture process with recurrence interval in a repeated small earthquake. Nature 368 (6472), 624–626. https://doi.org/10.1038/368624a0.

Viesca, R.C., 2016. Stable and unstable development of an interfacial sliding instability. Phys. Rev. E 93 (6), 1–6. https://doi.org/10.1103/PhysRevE.93.060202.